Unravelling the Key Relationship between Perovskite Capacitive Memory, Long Timescale Cooperative Relaxation Phenomena, and Anomalous *J–V* Hysteresis

Enrique Hernández-Balaguera,* Gonzalo del Pozo, Belén Arredondo, Beatriz Romero, Carlos Pereyra, Haibing Xie, and Mónica Lira-Cantú

Dr. Enrique Hernández Balaguera, Dr. Gonzalo del Pozo, Dr. Belén Arredondo, Prof. Beatriz Romero

Escuela Superior de Ciencias Experimentales y Tecnología, Universidad Rey Juan Carlos, C/ Tulipán, s/n, 28933 Móstoles, Madrid, Spain

E-mail: enrique.hernandez@urjc.es

Carlos Pereyra, Dr. Haibing Xie,Prof. Mónica Lira-Cantú

Catalan Institute of Nanoscience and Nanotechnology (ICN2), CSIC and the Barcelona Institute of Science and Technology, Campus UAB, 08193 Bellaterra (Barcelona), Spain

Keywords: perovskite solar cells, non-ideal capacitance, hysteresis, fractional calculus, impedance and transient analysis

Abstract

Capacitive response at long timescale seems to remain an elusive feature in the analysis of the electrical properties of perovskite-based solar cells. It belongs to one of the critical anomalous effects that arises from the characteristic phenomenology of this type of emerging photovoltaic devices. Thereby, accurately deducing key capacitance feature of new light harvesting perovskites from electrical measurements represents a significant challenge regarding the interpretation of physical processes and the control of undesired mechanisms, such as slow dynamic effects and/or current density-voltage (*J*–*V*) hysteresis. Here, it is shown that long timescale mechanisms that give rise to hysteresis in stable and high-efficiency quadruple-cation perovskites are not due to a classical capacitive behavior in the sense of ideal charge accumulation processes. Instead, it is a phenomenological consequence of slow memory-based capacitive currents and the underlying cooperative relaxations. This work reveals that a fractional dynamics approach, based on the idea of capacitance distribution in perovskite devices, reliably models the slow transient phenomena and the consequent scan-rate- and bias-dependent hysteresis. Observable for a wide variety of photovoltaic halide perovskites, distributed capacitive effects are rather universal anomalous phenomena, which can be related to the long-time electrical response and hysteresis.

Knowledge of the electrical properties of perovskite solar cells (PSCs) has gathered increasing interest in the photovoltaic research community because it helps to answer crucial questions about the unique phenomenology of this type of devices that still remain unsolved.[1] Certainly, determining appropriate correlations between the electrical response and the photophysical processes offers access to fundamental mechanisms of PSCs, and enables to unravel the distinctive electronic and ionic phenomena taking place during device operation, at different timescales.[2,3] Nevertheless, despite the intensive efforts to provide explanations upon the anomalous behaviors of PSCs (e.g., dynamic evolution of charge distributions, ubiquitous hysteresis, unusual relaxation processes),[4–6] there is still a lack of comprehension of the fundamental relationship between the physical aspects, electrical response, and theoretical modeling, ruling the device performance.[1,7] Of particular importance is the capacitance feature at long timescale, which may be the key mechanism responsible for such undesirable effects.[3,8,9] Thus, a reliable analysis of the electrical properties of PSCs, centered on the capacitive response, is one of the most important challenging goals in this field, in order to understand the rich and very complex phenomenology of this photovoltaic technology with respect to basic physics, operation principle, electrical behavior, and mathematical framework.

The term constant-phase element (CPE) is commonly used in electrical measurements (impedance spectroscopy, IS) to describe the anomalous low-frequency capacitive effects of photovoltaic perovskites.[10–13] Note that the impedance of a CPE is given by: $Z_{\mathrm{CPE}}(\mathrm{j}\omega)=1/Q(\mathrm{j}\omega)^{\alpha}$, where Q is the pseudo-capacitance, j is the imaginary unit, ω is the angular frequency related to the frequency by $\omega=2\pi f$, and α ($0<\alpha<1$) is the dispersion coefficient. In effect, the capacitive response of PSCs, at sufficiently low frequencies, varies inversely proportional to ($\mathrm{j}\omega$) but raised to an exponent α, which is below 1 ($\alpha=1$ for pure capacitive behavior). According to the properties of the complex

numbers, $j^{\alpha}=\cos\left(\alpha\pi/2\right)+j\sin\left(\alpha\pi/2\right)$, an alternative form for the CPE's impedance can be found: $Z_{CPE}(j\omega)=\left[\cos(\alpha\pi/2)/Q\omega^{\alpha}\right]-j\left[\sin(\alpha\pi/2)/Q\omega^{\alpha}\right]$,[14] which reveals that this element does not present entirely imaginary contributions (capacitive effects, $\alpha=1$), but contains both real and imaginary components (mixed resistive-capacitive properties, $0<\alpha<1$). Via inverse Laplace transform, the corresponding current density-voltage relationship in the time domain ($J_{CPE}(t)$-$v_{CPE}(t)$) is represented by the fractional-order differential equation:[15]

$$J_{CPE}(t)=Q\frac{d^{\alpha}v_{CPE}(t)}{dt^{\alpha}} \quad (1)$$

where Q has the units of $F/(cm^2s^{1-\alpha})$. d^{α}/dt^{α} ($0<\alpha<1$) is the fractional-order derivative of order α. This formalism, based on fractional operators, provides rather simple expressions in the frequency domain (fractionary exponents); however, it involves a non-intuitive modeling in the time domain.[16,17] Before proceeding any further, we should address the following question: Why is fractional calculus the adequate tool to model the complex phenomena of PSCs? In the context of literature, it has been demonstrated that fractional differential equations are a tailor-made approach for modelling the dynamic behavior of systems with structural complexity.[18–20] In particular, this mathematical tool has been used for systems that, furthermore, exhibit slow and persistent long-tailed memory phenomena (inverse power-law pattern) in transient measurements and pronounced deviations from the ideal capacitive behavior (Cole-Cole behavior) in IS,[21] both observed in PSCs. Taking into account this generalization, we are able to capture effectively, and without inconsistencies through linear and time invariant (LTI) theory, the well-established low-frequency dispersive behavior found in IS (CPE effects). Furthermore, since the electrical features of PSCs arise from the nanoscale device architecture and the underlying multiscale processes (e.g., redistribution of slowly

moving ions or carrier transport mechanisms),[2,22] the challenge for the perovskite's community is to develop new and accurate dynamic models that describe macroscale behavior from microscale mechanisms. These ideas make emerge the fractional calculus theory as a reliable theoretical background to model the complex dynamical phenomena that occur in PSCs and to control unfavorable phenomena, such as the current density-voltage (*J*–*V*) hysteresis.[23,24] The basic ideology of this branch of mathematics is to look at a fractional derivative as the inverse operation of a fractional integral, which is usually chosen as the Caputo form (i.e., ${}_0^C D_t^{\alpha} v_{\mathrm{CPE}}(t) = {}_0D_t^{-(1-\alpha)}[D v_{\mathrm{CPE}}(t)]$).[25] Thus, the time-fractional derivative can be defined as:

$$\frac{\mathrm{d}^{\alpha} v_{\mathrm{CPE}}(t)}{\mathrm{d}t^{\alpha}} = \frac{1}{\Gamma(1-\alpha)} \int_0^t (t-\tau)^{-\alpha} \frac{\mathrm{d}v_{\mathrm{CPE}}(\tau)}{\mathrm{d}\tau} \mathrm{d}\tau \tag{2}$$

Equation (2) demonstrates that the now-value of CPE's voltage can be found as the integral of ${\mathrm{d}v_{\mathrm{CPE}}(\tau)}/{\mathrm{d}\tau}$ (first-order derivative with a specific physical meaning) over all past values weighted by the kernel (or power-law scaling) function, ${(t-\tau)^{-\alpha}}/{\Gamma(1-\alpha)}$.[26] This dependence on the previous history (non-local property) contrasts with the integer-order derivative, which is assessed just instantaneously. Note that Γ is the Euler's Gamma function. Indeed, this theoretical perspective considers the "memory effects" of perovskite devices in a visualized manner due to the fact that the instantaneous change rate depends strongly on the past voltage activity. Lastly, it is important to point out that it exists a physically-based link between fractional calculus and fractal geometry (chaos),[27] which plays a relevant role in the underlying mechanisms that occur in nano-heterogeneous structures as those found in PSCs.

In a previous paper, the authors provided a theoretical framework for the transient-photocurrent analysis in stepwise–*JV* scanning (described by fractional-order responses)

to stablish a connection between perovskite memory effects, non-predictable or anomalous evolution of transient responses, CPE features in IS, structural complexity of PSCs, *J–V* hysteresis, and fractional dynamics.[23] Through this analysis, we showed that the non-ideal capacitive behavior (quantified by the dispersion coefficient α) and the corresponding distribution of time constants affects the transient dynamics of the current responses in *J–V* measurements, and even more important, the hysteresis events in a reversible manner. Certainly, in the vast majority of experimental scenarios, relaxation processes in PSCs deviate from the classical exponential pattern and thus, they should be described in terms of special functions (Mittag-Leffler function or asymptotic power-laws) that lead to an increased accuracy.[6,24,28] The occurrence of fractional relaxation functions and the underlying dynamics at multiple time scales in PSCs imply that the fundamental photovoltaic mechanisms are not unique to the device structure (cooperative relaxation phenomena, each one with its own characteristic time constant), but most likely reflect spatially distributed processes. In this sense, one should observe deviations from the linear scan-rate dependence of the capacitive hysteresis phenomena, which have been typically modeled as $J_{\mathrm{cap}}(V) = C\,{\Delta V}/{\Delta t} = Cs$,[9,29–31] obtaining the hallmark of fractional dynamics: The non-linear growth of the capacitive hysteretic currents with the increase of scan rate, and also, the decrease of initial poling conditions (perovskite's memory). In this report, we focus on the following power-law pattern[23]

$$J_{\mathrm{CPE}}(V) = Q\,\frac{\Delta V^{1-\alpha}}{\Gamma(2-\alpha)}\,s^{\alpha} \tag{3}$$

where *s* denotes the scan rate and ΔV (voltage shift) takes into account the pre-poling effect: $\Delta V = V - V_{\mathrm{pol}}$ (V_{pol} is the initial voltage or poling bias). Note that the conventional approach does not consider the initial pre-poling effect (see above). Thus, this ubiquitous expression is able to predict and control the reversible hysteretic effects observed in the *J–V* measurements taking into account: perovskite capacitive memory (electric mobility

of charged point-defects), anomalous dynamic (power-law decay), cooperative relaxation phenomena (distribution of time constants), and the physical picture of the underlying processes (long-tailed trapping events). Nevertheless, Equation (3) does not comprise all the variety of causes associated to the origin of the hysteresis.[32–34] Additional features, such as irreversible noncapacitive contributions of inverted nature, can be also obtained at slow enough scan rates (see below).

Here, we explore the fundamental role of dispersive (non-ideal) capacitive behavior in the hysteretic effects of novel quadruple-cation-based PSCs from *J–V* characteristics (in a wide range of scan rates and pre-poling bias) and impedance response. Among all extrinsic parameters affecting *J–V* hysteresis, pre-poling conditions and bias sweep speed have proven to be the most important, since they have a dramatic influence on the power conversion efficiency (PCE).[35,36] In our novel interpretation, based on a fractional (memory-based) dynamics approach, both factors have been taken into account in order to control the reversible capacitive-nature hysteretic currents. Inspired in novel architectures reported in recent studies,[37,38] we selected a quadruple-cation halide perovskite as the absorber which constitutes a highly attractive candidate for new efficient and stable light harvesting perovskites alternatives to conventional $CH_3NH_3PbI_3$ (MAPI). In effect, multiple-cation perovskite is one of the most advanced composition reported up to date in halide perovskite family, and is one of the candidates into clearing the hurdles to commercialization. We employ a halide perovskite with the formula $Rb_{0.05}Cs_{0.05}MA_{0.15}FA_{0.75}Pb_{1.05}(I_{0.95}Br_{0.05})_3$ since the fabricated PSCs results in devices with high efficiency (21 %, see Supporting Information) and able to deliver high stability in our laboratory (> 1000 h under continuous light irradiation) [Ref: H. Xie, et al, 2020, submitted]. The anomalous hysteresis behavior and photovoltaic performance of our quadruple-cation perovskite has been tested fabricating an n-i-p type stack configuration

with *spiro*-OMeTAD as the hole transporting material and compact-TiO_2/mesoporous TiO_2 layer as the electron selective contact (refer to **Figure 1**a), following the method described in Experimental Section of the Supporting Information. This paper provides a detailed analysis to interpret and model the key capacitive features and distinctive physical mechanisms of perovskite-based solar cells in the context of reversible hysteresis effects and long-time responses. Thus, results obtained from this work contribute to gain further knowledge of the characteristic phenomenology of PSCs, with the aim of comprehensively covering recent advances in novel structures.

To clarify the nature of the capacitive hysteretic currents underlying reversible processes (predominance of bulk processes, ionic and electronic charge accumulation at the TiO_2/perovskite interface), we have analyzed the effect of the scan rate and the pre-poling voltage bias, in the *J–V* curve of our PSCs in dark conditions. Despite light irradiation influences hysteresis, it is not the fundamental cause of this anomalous phenomenon,[39] and thus, in order to avoid cell heating or nonstabilized illumination effects (in terms of degradation processes), we have developed experiments in dark. Firstly, *J–V* curves have been registered covering a wide range of scan rates (ranging from 250 down to 0.5 mV/s). In general, hysteretic currents appear superimposed to the operational current, i.e., $J(V) = J_{\mathrm{oper}}(V) + J_{\mathrm{hyst}}(V)$, which is the basis of the origin of hysteresis phenomena.[7,29] For convenience, $J_{\mathrm{hyst}}(V)$ can be expanded in terms of capacitive-based (normal) $J_{\mathrm{CPE}}(V)$ and noncapacitive (inverted) $J_{\mathrm{noncap}}(V)$ hysteretic currents, in order to provide a qualitative description of the vast majority of effects associated to anomalous hysteresis: $J_{\mathrm{hyst}}(V) = J_{\mathrm{CPE}}(V) + J_{\mathrm{noncap}}(V)$. The general behavior of hysteretic currents with scan rate ($J_{\mathrm{hyst}}(V)$-*s*, see **Figure 1**b), which could be considered as a "universal" map to control hysteresis effects, exhibits well-separated scan-rate-dependent scales.[23] Theoretically, at sufficiently high measuring speeds

($s\rightarrow\infty$), the influence of dynamic transient contributions on the hysteresis effects is negligible because the electrical inertia of the perovskite (distributed time-constant, τ) is much greater than the delay time between measurement points: $\Delta t<<\tau$. That is, the charging phenomena of the CPE is limited via $(R_{Th}Q)^{1/\alpha}$ –R_{Th} is the Thévenin resistance–, involving that hysteresis effects fade. Note that preservation of linearity conditions (constant voltage-steps) is assumed. It is worth mentioning that capacitive effects show a dual behavior: peak capacitive current ($\Delta t\rightarrow 0$) and slow transient process.[40] In this scenario, each current data point represents the peak value of the non-steady-state current (of iR-drop nature). Nevertheless, the introduction of CPEs involves Mittag-Leffler decays (initial fast stretched exponential pattern if $\Delta t\rightarrow 0$) for each step during the stepwise scanning, instead of classical exponential functions (at $\Delta t\rightarrow 0$, linear time-dependent response).[16] This, in turn, results in longer scan rates for transient effects to be vanished. The physical meaning associated to this measurement protocol can be related to the fact that, during short timescales, the space charge regions do not have enough time to change due to slow-moving ions.[41] As the applied scan rate decreases (so that Δt is comparable to τ), $J_{CPE}(V)$ abruptly emerges and gradually reduces because the measuring voltage speed approaches the steady-state conditions. **Figure 1**c shows that the CPE charging phenomena at non-steady-state levels distort the *J*–*V* curve, $J_{hyst}(V) \rightarrow J_{CPE}(V)$, between 250 and 5 mV/s. Note that non-ideal capacitive hysteretic currents are clearly visible at low voltages (in the voltage range ranging from –0.3 down to 0.6 V) because $J_{oper}(V)<<J_{CPE}(V)$ or $J_{oper}(V)\sim J_{CPE}(V)$. In the high voltage range (>0.6 V), the operational current collapses into a single response –the final currents for both forward and reverse sweep directions are equal to the steady-state values, $J_{oper}(V)>>J_{CPE}(V)$–. Unlike the conventional PSCs comprising TiO_2 as electron collecting material,[7,9,31] our devices show a non-linear relationship (power-law pattern, see Equation (3)) between the scan

rate and the capacitive-nature hysteretic currents ($J_{CPE}(V)$-*s*, refer to **Figure 1**d), where α=0.874 and *Q*=16.92 μF/(cm^{2}s$^{1-\alpha}$). Note that excess of capacitive contributions has been evaluated at zero volts as: $J_{\mathrm{CPE}}(0) = J(0) - J_{\mathrm{oper}}(0)$, being $J_{oper}(0)$ the current of slowest swept evaluated at *V*=0 V. Analogously to the region dominated by the response limitation of the fractional-order capacitor (*s*→∞), the non-exponential dynamics imposed by CPE effects (terminal inverse power-law decay for Δ*t*→∞) lead to non-fully inhibition of the anomalous hysteresis. In contrast, the transient component is reduced to <1% at Δ*t*=5τ if one considers an ideal exponential behavior.[17] This unexpected pattern can be explained on the basis of the electrical representation of a CPE,[42] involving equivalent networks constituted by an infinite number of RC sub-circuits (fractal networks) and, in turn, leads to an adequate interpretation of the underlying cooperative relaxation mechanisms involved in PSCs.[28] Finally, at sufficiently low scan rates (*s*→0: 0.5 and 1 mV/s), *J*–*V* curve distortions, in the form of inverted hysteresis effects (of noncapacitive origin),[29,31] appear according to the theoretically predicted trend (see Figure 1b), instead of a hysteresis-free steady-state dark *J*–*V* curve; i.e., Δ*t*>>τ, but $J_{\mathrm{hyst}}(V) \rightarrow J_{\mathrm{noncap}}(V)$. As can be seen in **Figure 1**e, in contrast to capacitive hysteresis behavior, noncapacitive hysteretic currents increase as the scan rate decreases, which is one of the hallmarks of noncapacitive distortions. Note that these prominent contributions to the overall hysteretic response arise around 0.1-0.7 V at both forward and reverse voltage sweeps. As suggested in previous works, the underlying mechanisms behind the noncapacitive hysteresis are related to the reactivity between mobile ions of the perovskite at the interface (e.g., iodine anions, I^-) and the hole transport layer (*spiro*-OMeTAD$^+$).[43] Thus, they can be assimilated as the Faradaic currents commonly found in Electrochemistry (i.e., mathematically modelled as Nernst-Monod or Butler-Volmer equations) and/or recombination processes due to modified space charge regions.[29]

Nevertheless, the exact origin of this effect in our devices is beyond the scope of this work.

Next, we analyze the dependence of the hysteretic distortions on the bias pre-poling, by considering fractional dynamics of the relaxation process occurring at long timescale. The sketch of **Figure 2**a shows the different regions of influence of $J_{CPE}(V)$ depending on the voltage variation ΔV and the CPE-parameter, at constant s: (i) Hysteresis undergoes an enlargement when the voltage sweep starts from a more negative bias voltage ($J_{CPE}(V)$ increases with ΔV),[44,45] which is in sharp contrast with the pure capacitive current – $J_{cap}(V)$– resembling a bias-independent square loop.[9] (ii) The CPE-nature hysteretic currents dramatically increase with the decrease of the fractional-order α.[24] Both effects can be easily verified through Equation (3). **Figure 2**b illustrates a representative example of the experimental dark *J–V* curves of the quadruple-cation photovoltaic perovskites at different scanning bias conditions (ranging from –1, –0.3, or –0.2 V to 1 V) for a fixed voltage sweep rate (25 mV/s). Results shown in Figure 2b are in good agreement with the previous remarks: Capacitive-nature hysteretic currents can be certainly dealt as CPE-based distortions due to its non-linear dependence with the scanning bias voltage (see inset of Figure 2b), and also, because they accurately model the experimental outcomes based on memory effects of PSCs. This characteristic behavior (power-law pattern) is plotted in **Figure 2**c, obtaining α=0.856 and Q=20.81 μF/(cm^{2}s$^{1-\alpha}$).

In order to reinforce the previous hysteresis analysis, a comparison test was carried out through impedance measurements. Basically, this technique consists of sequentially injecting small AC perturbations (single-sinusoidal signals) superimposed to a DC bias point, typically voltage, sweeping the frequency over a range of interest (from several mHz up to 1 MHz), and measuring the resulting current at each frequency (impedance response).[46] From the resulting spectra, it is possible to easily separate the resistive and

capacitive contributions even for deformed arcs (distributed electrical equivalent circuits) or complicated IS spectra (e.g., inductive elements or so-called negative capacitances). IS analysis for quadruple-cation-based PSCs in dark conditions is shown in Figure 3; Capacitance Bode representation: **Figure 3**a, and Nyquist plot: **Figure 3**b. In these plots, Z' and Z'' are the real and imaginary parts of the impedance, respectively, and C is the capacitance. In the high-frequency range, the capacitance-frequency plot appears as a straight line with zero slope, and the impedance spectrum outlines a perfect semicircle whose center lays on the Z'-axis, indicating an ideal capacitive behavior associated to a relaxation process $-\tau_{HF}=R_{HF}C_{HF}=94.14$ μs–. This characteristic capacitance (so-called geometrical capacitance, here C_{HF}) can be attributed to the dielectric response of the perovskite layer (unaffected by the irradiation intensity).[7,47] On the other hand, IS spectra showed a CPE-like behavior at low frequencies (CPE_{LF}), characterized by a slanted capacitance defined as

$$C_{LF}(\omega) = Q\omega^{\alpha-1}\cos\left[(\alpha-1)\frac{\pi}{2}\right] \quad (4)$$

and a depressed symmetrical semicircular arc in the Nyquist plot $-\tau_{LF}=(R_{LF}Q)^{1/\alpha}=26.49$ s–. Note that Equation (4) can be obtained from the expression of the complex capacitance, $C(\omega) = {}^{1}/_{j\omega[Z(\omega)-R_S]}$,[48] being $[Z(\omega)–R_S]$ the impedance of the low-frequency R-CPE subcircuit. In effect, this tendence suggests a deviation from the ideal capacitive behavior, generally due to dispersion of the time constant caused by irregularities on the contact surfaces, bulk roughness, fractal surface and, more generally, mechanisms associated with a non-uniform distribution of the applied voltage.[49] Note that this capacitance feature, in dark conditions, is related to the electrode polarization taking place as a consequence of ion interfacial accumulation and hence restricted to the space charge region width (thickness-independent pattern).[9,40] Thus, from the raw observations of the experimental data, the system appeared to be defined by two

relaxation events. Among the various reported electrical models describing IS spectra,[7,47,50–52] we have selected, for simplicity (physical meaning) and effectiveness (relation between the electrical response and the characteristic phenomenology of the solar cells), the Matryoshka equivalent circuit, shown in **Figure 3**c. In addition to the series resistance R_S (which shifts the arcs positively along the real axis), the electrical model comprises a C_{HF} in parallel with a high-frequency resistance (R_{HF}), and the latter in series with one R-CPE network (a low-frequency resistance R_{LF} and a CPE_{LF} taking into account the non-ideal capacitive behavior of perovskite devices). CPE_{LF} has been highlighted in yellow in the circuit, and can be correlated with anomalous electronic and ionic dynamics. Furthermore, **Figure 3**d shows an equivalent network model of the CPE_{LF} by way of illustration, representing the influence of modifying electrode polarization on capacitive effect. Finally, in **Figure 3**e, we present a representative example of the dynamic $J(t)$ transient response in the context of stepwise-JV measurements. For this case, i.e., a voltage-controlled technique, the time constants correspond to the characteristic frequencies of the admittance response, τ_{ST}~$R_S C_{HF}$ and τ_{LT}~$[(R_{HF}//R_{LF})Q]^{1/\alpha}$, which govern the initial decay-exponential region (at sufficiently short times) and the long-timescale non-exponential behavior of the current density, respectively.[24] A basic exploration of the resulting response shows that the overall relaxation process (τ_{LT}>>τ_{ST}) is described in terms of the one-parameter Mittag-Leffler function, yielding

$$J(t) - J_\infty = J_Q \sum_{k=0}^{\infty} \frac{\left[-\left(\frac{t}{\tau_{LT}}\right)^{\alpha}\right]^k}{\Gamma(\alpha k + 1)} = J_Q \mathrm{E}_\alpha\left[-\left({}^{t}/_{\tau_{LT}}\right)^{\alpha}\right]$$
$$\approx \begin{cases} J_Q \exp\left[-\dfrac{\left({}^{t}/_{\tau_{LT}}\right)^{\alpha}}{\Gamma(\alpha+1)}\right], & t << \tau_{LT} \\ J_Q \dfrac{\left({}^{t}/_{\tau_{LT}}\right)^{-\alpha}}{\Gamma(1-\alpha)}, & t >> \tau_{LT} \end{cases} \quad (5)$$

where J_∞ is the steady-state response and J_Q is the value of the current density immediately after the appearance of the CPE effects. For $\alpha=1$, $J(t)-J_\infty$ follows the standard exponential form, whereas for $0<\alpha<1$, the initial stretched exponential behavior turns over to a power-law long-time behavior.[21,53] In effect, the ubiquitous Mittag-Leffler function interpolates between an initial Kohlrausch-Williams-Watts (KWW) and a final inverse power-law decay. Note that the full theory behind the stepwise-*JV* measurements and further details of its experimental application, using fractional calculus, are described in previous works of the authors.[23,24] Since the characteristic parameter values of long-term capacitance feature obtained using IS $-Q=18.28$ $\mu F/(cm^2 s^{1-\alpha})$ and $\alpha=0.876$– are remarkably close to those found from *J*–*V* characteristics, we conclude that our modeling is consistent and confirms the validity of the long timescale and anomalous hysteresis model previously discussed.

The unprecedentedly rapid emergence and subsequent consolidation of a new class of photovoltaic devices based on perovskite materials have revolutionized the third-generation solar cells. The characteristic phenomenology of perovskite cells, in terms of key attributes and a very broad set of unique physical mechanisms, leads to new opportunities, future prospects, and crucial challenges for further progress in this highly-efficient photovoltaic technology. In this work, we have shown that the origin of the capacitive feature at long timescale in a novel quadruple-cation perovskite is not due to standard mechanisms (ionic and electronic charge accumulation) but due to cooperative phenomena, described mathematically in terms of distributed relaxation processes (dispersion of capacitance). Consequently, its appearance correlates with the reversible phenomena associated to *J*–*V* hysteresis. Through the paper, we show that a fractional dynamics approach is able to accurately model anomalous hysteresis mechanisms in perovskite-based solar cells, allowing a precise description of the capacitive features and

dynamic of relaxation processes (CPE effects). In order to clarify discussions about distinct trends observed in experimental transient responses, our analysis on the impedance and capacitance features of PSCs takes into account: the non-linear tendency of the capacitive-nature hysteretic currents with the measuring speed (power-law pattern), the bias-dependent characteristic (perovskite memory), and the constant phase behavior (long tail of the current) in the frequency (time) domain. The combination of accurate mathematical models and the in-depth understanding on the specific and differential capacitive properties of perovskite-based solar cells will help to optimize measurement protocols for the dynamic *J–V* characteristic and, consequently, provide an estimation of the solar energy conversion efficiency.

Supporting Information

Supporting Information is available from the Wiley Online Library or from the author.

Acknowledgements

This work has been supported by Comunidad de Madrid under the SINFOTON2-CM Research Program, S2018/NMT4326-SINFOTON2-CM, the Ministerio de Economía, Industria y Competitividad, Project TEC2016-77242-C3-3-R, and the European Regional Development Fund (fondos FEDER). To the Ministerio de Ciencia e Innovación for the grant GraPErOs (ENE2016-79282-C5-2-R) and the Self-Power (PID2019-104272RB-C54). To the Agència de Gestiód'Ajuts Universitaris i de Recerca (AGAUR) for the support to the consolidated Catalonia research group 217 SGR 329 and the Xarxa d'R+D+I Energy for Society (XRE4S). Part of this work is under Materials Science Ph.D. Degree for C.P. of the Universitat Autónoma de Barcelona. We thank CONACYT for the

scholarship to C.P. ICN2 is supported by the Severo Ochoa program from MINECO (SEV-2017-0706) and is funded by the CERCA Programme/Generalitat de Catalunya.

Received: ((will be filled in by the editorial staff))
Revised: ((will be filled in by the editorial staff))
Published online: ((will be filled in by the editorial staff))

References

[1] P. Lopez- Varo, J. A. Jiménez- Tejada, M. García- Rosell, S. Ravishankar, G. Garcia- Belmonte, J. Bisquert, O. Almora, *Adv. Energy Mater.* **2018**, *8*, 1702772.

[2] H. Wang, A. Guerrero, A. Bou, A. M. Al-Mayouf, J. Bisquert, *Energy Environ. Sci.* **2019**, *12*, 2054.

[3] R. S. Sanchez, V. Gonzalez-Pedro, J.-W. Lee, N.-G. Park, Y. S. Kang, I. Mora-Sero, J. Bisquert, *J. Phys. Chem. Lett.* **2014**, *5*, 2357.

[4] P. Lopez-Varo, J. A. Jiménez-Tejada, M. García-Rosell, J. A. Anta, S. Ravishankar, A. Bou, J. Bisquert, *ACS Energy Lett.* **2017**, *2*, 1450.

[5] H. J. Snaith, A. Abate, J. M. Ball, G. E. Eperon, T. Leijtens, N. K. Noel, S. D. Stranks, J. T.-W. Wang, K. Wojciechowski, W. Zhang, *J. Phys. Chem. Lett.* **2014**, *5*, 1511.

[6] E. L. Unger, E. T. Hoke, C. D. Bailie, W. H. Nguyen, A. R. Bowring, T. Heumüller, M. G. Christoforo, M. D. McGehee, *Energy Environ. Sci.* **2014**, *7*, 3690.

[7] O. Almora, K. T. Cho, S. Aghazada, I. Zimmermann, G. J. Matt, C. J. Brabec, M. K. Nazeeruddin, G. Garcia-Belmonte, *Nano Energy* **2018**, *48*, 63.

[8] E. J. Juarez-Perez, R. S. Sanchez, L. Badia, G. Garcia-Belmonte, Y. S. Kang, I. Mora-Sero, J. Bisquert, *J. Phys. Chem. Lett.* **2014**, *5*, 2390.

[9] O. Almora, I. Zarazua, E. Mas-Marza, I. Mora-Sero, J. Bisquert, G. Garcia-Belmonte, *J. Phys. Chem. Lett.* **2015**, *6*, 1645.

[10] L. Contreras-Bernal, S. Ramos-Terrón, A. Riquelme, P. P. Boix, J. Idígoras, I. Mora-Seró, J. A. Anta, *J. Mater. Chem. A* **2019**, *7*, 12191.

[11] E. von Hauff, *J. Phys. Chem. C* **2019**, *123*, 11329.

[12] A. Pockett, G. E. Eperon, T. Peltola, H. J. Snaith, A. Walker, L. M. Peter, P. J. Cameron, *J. Phys. Chem. C* **2015**, *119*, 3456.

[13] A. Todinova, L. Contreras- Bernal, M. Salado, S. Ahmad, N. Morillo, J. Idígoras, J. A. Anta, *ChemElectroChem* **2017**, *4*, 2891.

[14] J. Ross Macdonald, *Solid State Ion.* **1984**, *13*, 147.

[15] S. Westerlund, L. Ekstam, *IEEE T. on Dielect. El. In.* **1994**, *1*, 826.

[16] E. Hernández-Balaguera, J. L. Polo, *Electrochim. Acta* **2017**, *233*, 167.

[17] E. Hernández-Balaguera, J. L. Polo, *J. Electroanal. Chem.* **2020**, *856*, 113631.

[18] R. Hilfer, *Applications of Fractional Calculus in Physics*; World Scientific, 2000.

[19] R. Metzler, J. Klafter, *Phys. Rep.* **2000**, *339*, 1.

[20] R. L. Magin, *Fractional Calculus in Bioengineering*; Begell House, 2006.

[21] R. Metzler, J. Klafter, *J. Non-Cryst. Solids* **2002**, *305*, 81.

[22] A. Pockett, G. E. Eperon, N. Sakai, H. J. Snaith, L. M. Peter, P. J. Cameron, *Phys. Chem. Chem. Phys.* **2017**, *19*, 5959.

[23] E. Hernández-Balaguera, B. Arredondo, G. del Pozo, B. Romero, *Commun. Nonlinear Sci. Numer. Simulat.* **2020**, *90*, 105371.

[24] E. Hernández-Balaguera, B. Romero, B. Arredondo, G. del Pozo, M. Najafi, Y. Galagan, *Nano Energy* **2020**, *78*, 105398.

[25] I. Podlubny, *Fractional Differential Equations: An Introduction to Fractional Derivatives, Fractional Differential Equations, to Methods of Their Solution and Some of Their Applications*; Academic Press, 1998.

[26] A. Allagui, D. Zhang, I. Khakpour, A. S. Elwakil, C. Wang, *J. Phys. D: Appl. Phys.* **2019**, *53*, 02LT03.

[27] S. Butera, M. Di Paola, *Ann. Phys.* **2014**, *350*, 146.

[28] L. Bertoluzzi, R. S. Sanchez, L. Liu, J.-W. Lee, E. Mas-Marza, H. Han, N.-G. Park, I. Mora-Sero, J. Bisquert, *Energy Environ. Sci.* **2015**, *8*, 910.

[29] O. Almora, C. Aranda, I. Zarazua, A. Guerrero, G. Garcia-Belmonte, *ACS Energy Lett.* **2016**, *1*, 209.

[30] M. Vallés-Pelarda, B. Clasen Hames, I. García-Benito, O. Almora, A. Molina-Ontoria, R. S. Sánchez, G. Garcia-Belmonte, N. Martín, I. Mora-Seró, *J. Phys. Chem. Lett.* **2016**, *7*, 4622.

[31] G. Garcia-Belmonte, J. Bisquert, *ACS Energy Lett.* **2016**, *1*, 683.

[32] B. Chen, M. Yang, S. Priya, K. Zhu, *J. Phys. Chem. Lett.* **2016**, *7*, 905.

[33] P. Liu, W. Wang, S. Liu, H. Yang, Z. Shao, *Adv. Energy Mat.* **2019**, *9*, 1803017.

[34] N. K. Elumalai, A. Uddin, *Sol. Energy Mater. Sol. Cells* **2016**, *157*, 476.

[35] J. A. Christians, J. S. Manser, P. V. Kamat, *J. Phys. Chem. Lett.* **2015**, *6*, 852.

[36] G. A. Nemnes, C. Besleaga, A. G. Tomulescu, A. Palici, L. Pintilie, A. Manolescu, I. Pintilie, *Sol. Energy* **2018**, *173*, 976.

[37] M. Saliba, T. Matsui, K. Domanski, J.-Y. Seo, A. Ummadisingu, S. M. Zakeeruddin, J.-P. Correa-Baena, W. R. Tress, A. Abate, A. Hagfeldt, M. Grätzel, *Science* **2016**, *354*, 206.

[38] Y. Hu, E. M. Hutter, P. Rieder, I. Grill, J. Hanisch, M. F. Aygüler, A. G. Hufnagel, M. Handloser, T. Bein, A. Hartschuh, K. Tvingstedt, V. Dyakonov, A. Baumann, T. J. Savenije, M. L. Petrus, P. Docampo, *Adv. Energy Mater.* **2018**, *8*, 1703057.

[39] W. Tress, N. Marinova, T. Moehl, S. M. Zakeeruddin, M. K. Nazeeruddin, M. Grätzel, *Energy Environ. Sci.* **2015**, *8*, 995.

[40] B. Chen, M. Yang, X. Zheng, C. Wu, W. Li, Y. Yan, J. Bisquert, G. Garcia-Belmonte, K. Zhu, S. Priya, *J. Phys. Chem. Lett.* **2015**, *6*, 4693.

[41] G. Richardson, S. E. J. O'Kane, R. G. Niemann, T. A. Peltola, J. M. Foster, P. J. Cameron, A. B. Walker, *Energy Environ. Sci.* **2016**, *9*, 1476.

[42] B. Hirschorn, M. E. Orazem, B. Tribollet, V. Vivier, I. Frateur, M. Musiani, *Electrochim. Acta* **2010**, *55*, 6218.

[43] J. Carrillo, A. Guerrero, S. Rahimnejad, O. Almora, I. Zarazua, E. Mas- Marza, J. Bisquert, G. Garcia- Belmonte, *Adv. Energy Mater.* **2016**, *6*, 1502246.

[44] X. Cao, Y. Li, C. Li, F. Fang, Y. Yao, X. Cui, J. Wei, *J. Phys. Chem. C* **2016**, *120*, 22784.

[45] F. Wu, B. Bahrami, K. Chen, S. Mabrouk, R. Pathak, Y. Tong, X. Li, T. Zhang, R. Jian, Q. Qiao, *ACS Appl. Mater. Interfaces* **2018**, *10*, 25604.

[46] E. Barsoukov, J. Ross Macdonald, *Impedance Spectroscopy: Theory, Experiment, and Applications*; John Wiley & Sons, 2005.

[47] I. Zarazua, G. Han, P. P. Boix, S. Mhaisalkar, F. Fabregat-Santiago, I. Mora-Seró, J. Bisquert, G. Garcia-Belmonte, *J. Phys. Chem. Lett.* **2016**, *7*, 5105.

[48] H. Liao, W. Watson, A. Dizon, B. Tribollet, V. Vivier, M. E. Orazem, *Electrochim. Acta* **2020**, *354*, 136747.

[49] J.-B. Jorcin, M. E. Orazem, N. Pébère, B. Tribollet, *Electrochim. Acta* **2006**, *51*, 1473.

[50] W. Peng, C. Aranda, O. M. Bakr, G. Garcia-Belmonte, J. Bisquert, A. Guerrero, *ACS Energy Lett.* **2018**, *3*, 1477.

[51] A. Guerrero, G. Garcia-Belmonte, I. Mora-Sero, J. Bisquert, Y. S. Kang, T. J. J acobsson, J.-P. Correa-Baena, A. Hagfeldt, *J. Phys. Chem. C* **2016**, *120*, 8023.

[52] E. Ghahremanirad, A. Bou, S. Olyaee, J. Bisquert, *J. Phys. Chem. Lett.* **2017**, *8*, 1402.

[53] F. Mainardi, *Discrete Contin. Dyn. Syst. Ser. B* **2014**, *19*, 2267

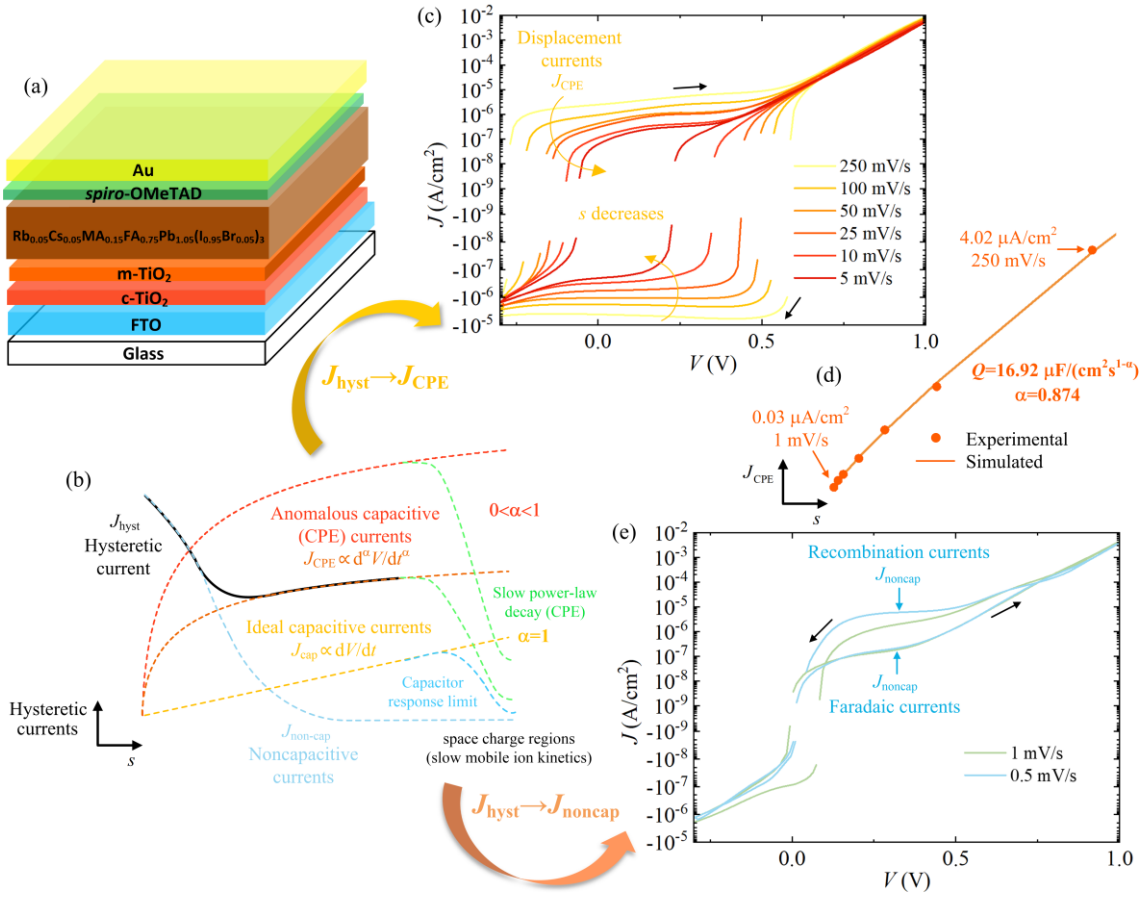

Figure 1. (a) Configuration of the quadruple-cation halide perovskite solar cell (PSC) analyzed in this work. (b) Schematic illustration of the origin of current density-voltage (J−V) hysteresis behavior depending on the scan rate. Three fundamental regions of influence of hysteretic currents are shown: The (non-)ideal capacitor response limit, the ideal or (c) anomalous capacitive effects in the middle dynamic range –(d) with the non-linear relationship between anomalous capacitive (constant phase element, CPE) current, $J_{CPE}(V)$, and the scan rate, s, at 0 V−, and (e) noncapacitive contributions at low enough scan rates. All dark J−V curves are shown in logarithm scaled currents representation. Black arrows indicate the scan direction.

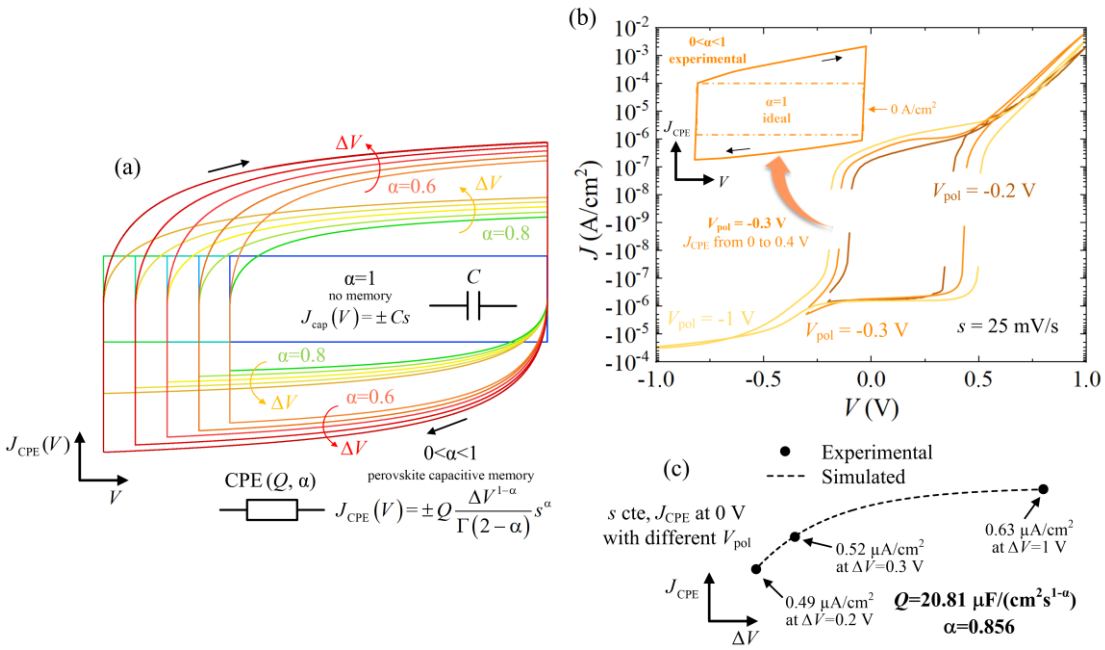

Figure 2. (a) Sketch of general behavior of $J_{CPE}(V)$ as a function of pre-poling bias conditions (perovskite capacitive memory), CPE parameter, and applied voltage. (b) Experimental dark J–V characteristics in logarithmic scaled current representation obtained after pre-poling the devices at different voltages (−1, −0.3, or −0.2 V), using a middle-range scan rate (25 mV/s). Inset: Illustrative example of the tendence of $J_{CPE}(V)$, extracted from J–V curve for V_{pol}=−0.3 V, at different applied voltages. (c) $J_{CPE}(V)$ versus voltage shift ΔV, obtained as in inset of Figure 2b, at zero volts.

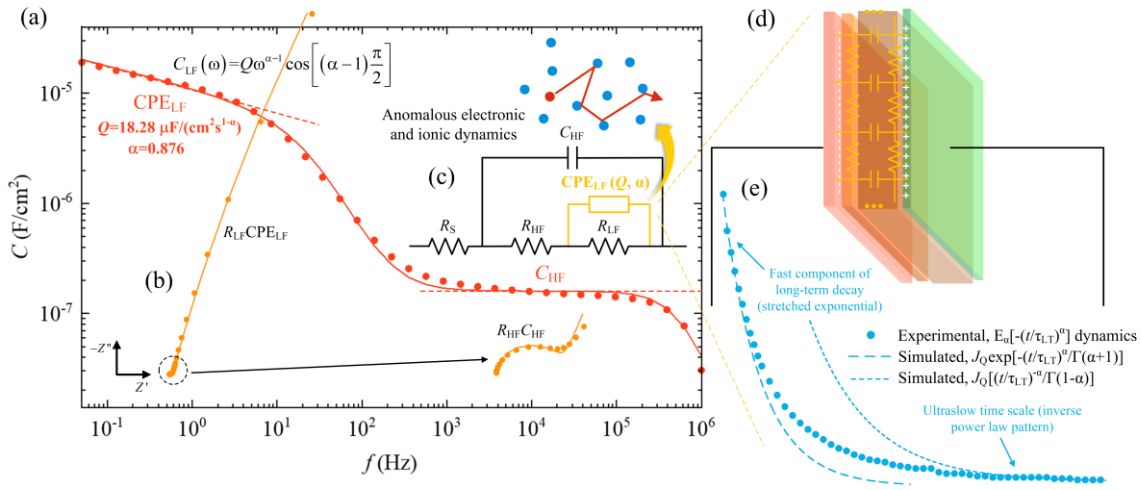

Figure 3. In dark conditions and 0 V, (a) representative example of the capacitance (Bode plot) and (b) impedance (Nyquist plot) for the quadruple-cation halide PSC at zero bias voltage. Inset in (b) shows the low-frequency range. In (a) and (b), the main capacitive-nature and resistive effects are highlighted. (c) Electrical equivalent circuit used to model impedance spectra, where the appearance of the key circuit element (CPE$_{LF}$), in the context of anomalous mechanisms of PSCs, is attributed to the anomalous ionic and electronic dynamics (fractional calculus approach). (d) Impact of electrode polarization on CPE effects and the subsequent dynamic $J(t)$ transient processes −see illustrative example of (e)− characterized by the persistent long-range time current.

The table of contents entry

One of the remaining crucial hurdles on the path to successful commercialization of perovskite-based solar cells is the in-depth understanding of its inherent characteristic phenomenology, particularly concerning the long timescale. From a fresh perspective, our work explores the primary factors governing this anomalous behavior (slow charge dynamics, long-memory processes, and hysteresis) and its key interrelationship, in order to cover recent advances and progress further in the performance enhancement of novel photovoltaic perovskites.

Enrique Hernández-Balaguera,* Gonzalo del Pozo, Belén Arredondo, Beatriz Romero, Carlos Pereyra, Haibing Xie, Mónica Lira-Cantú

Unravelling the Key Relationship between Perovskite Capacitive Memory, Long Timescale Cooperative Relaxation Phenomena, and Anomalous *J–V* Hysteresis

ToC figure

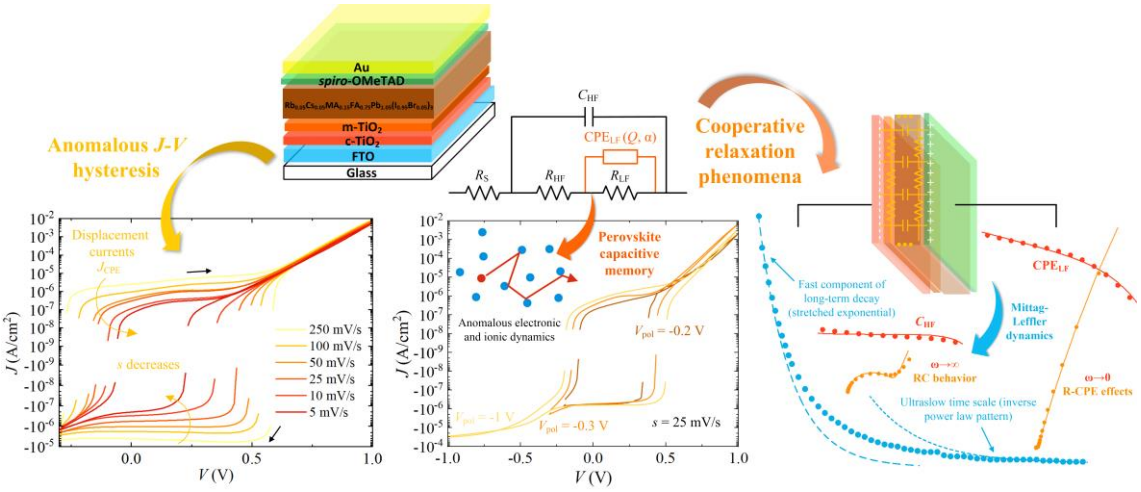

Supporting Information

Unravelling the Key Relationship between Perovskite Capacitive Memory, Long Timescale Cooperative Relaxation Phenomena, and Anomalous *J–V* Hysteresis

Enrique Hernández-Balaguera,* Gonzalo del Pozo, Belén Arredondo, Beatriz Romero, Carlos Pereyra, Haibing Xie, and Mónica Lira-Cantú

Experimental Methods

Fabrication. FTO substrates (Nippon Sheet Glass 10 Ω/sq) were etched by Zn powder and 4 M HCl, and then were cleaned with Hellmanex®, acetone and ethanol for 15 min, respectively inside an ultrasonic bath, finally were immediately dried with dry air. Compact TiO_2 (c-TiO_2) solution was prepared with titanium diisopropoxide bis(acetylacetonate):acetylacetone:ethanol=0.6:0.4:9 (v:v) and then were sprayed onto FTO substrates at 450 °C. Mesoporous TiO_2 (m-TiO_2) paste was prepared with titanium paste:ethanol=1:6 (w:w), and was spin coated to c-TiO_2 substrates at 5000 rpm for 20 s and then annealed at 450 °C for 30 min. After that, the as-prepared FTO/c-TiO_2/m-TiO_2 substrates were quickly transferred to a N_2 filled glove box for perovskite and *spiro*-OMeTAD deposition (no post-treatments were conducted for the substrates before deposition). The quadruple cation halide perovskite $Rb_{0.05}Cs_{0.05}MA_{0.15}FA_{0.75}Pb_{1.05}(I_{0.95}Br_{0.05})_3$ was prepared as follows. Briefly, first 1.5 M stock solution of 1) CsI (DMSO), 2) RbI (DMSO), and 3) PbI_2 (DMSO:DMF=1:4) were prepared, respectively. Then 1.5 M 4) $(MABr)_{0.9}(PbI_2)$ (DMSO:DMF=1:4), and 5) $(FAI)_{0.9}(PbI_2)$ (DMSO:DMF=1:4) were freshly prepared by dissolving MABr or FAI power in solution 3), respectively. After that, the solutions were mixed at a ratio of

4):5):1):2):3)=190:950:60:60:60 (v:v) in sequence. The perovskite spin coating process was carried out at 2000 rpm for 10 s, and then 6000 rpm for 30 s. Initially, 50 μL perovskite solution was dropped on a 1.5×2.5 cm^2 FTO/c-TiO_2/m-TiO_2 substrate. During the second step of spin coating, 100 μL chlorobenzene was dropped at 15 s before ending. The samples were annealed at 100 °C for 1 h on a hot plate for crystallization. Hole transporting layer was prepared by dissolving 0.12 g *spiro*-OMeTAD in 1130 μL chlorobenzene and then doped with 47.3 μL TBP and 23.5 μL Li-TFSI (1.8 M in acetonitrile). The spin coating was conducted at 4000 rpm for 20 s with 50 μL solution. The finished devices were placed inside a dry air box for 12 h to fully oxidize the *spiro*-OMeTAD. Finally, 80 nm Au was deposited as the front electrode by thermal evaporation. The evaporation rate was controlled in different stages to limit the damage to the *spiro*-OMeTAD layer: 0.003 nm/s for 0-1nm, 0.01 nm/s for 1-10 nm, 0.02 nm/s for 10-20 nm and 0.06 nm/s for 20-80 nm.

Characterization. Electrical measurements were carried out using an AutoLab potentiostat/galvanostat model PGSTAT204 (Eco-Chemie), equipped with the FRA32M impedance module. The instrument was controlled by a computer and driven by the NOVA 2.1.4 software. Illuminated current density-voltage (*J*−*V*) characteristics were obtained by performing a cyclic voltammetry test from −0.3 to 1.2 V, under AM1.5 100 mW/cm^2 simulated sunlight (Newport VeraSol-2 light-emitting diode, LED, class AAA) previously calibrated with an NIST-certified KG3 filtered Si reference cell. The obtained solar cell parameters, using a 0.16 cm^2 mask, were: V_{OC}=1.10 V, J_{SC}=20.96 mA/cm^2, FF=75.49%, PCE=17.41%; assessed under a slow voltage sweep velocity (10 mV/s). Dark *J*−*V* curves were measured, in order to check hysteresis behavior, with a 10 mV step at different scan rates (ranging from 250 down to 0.5 mV/s) from −1, −0.3, or −0.2 V to 1 V. Chronoamperometric experiments were carried out by configuring the Autolab to

apply piecewise-constant signals with a delay time of 1 s and voltage-excited steps of 10 mV. A sampling rate of 1 MHz was used to record an accurate current response. The fitting procedure was performed using MATLAB routines for assessing the non-classical relaxation processes.[1,2] Impedance measurements were carried out immediately after *J*−*V* experiments, by configuring the AutoLab to apply sinusoidal signals of 10 mV amplitude from 1 MHz to 50 mHz at constant zero bias voltage (short circuit conditions). Fitting of all of the impedance spectra was performed using Scribner's ZView software. The reproducibility of experimental data was checked and assured by conducting *J*−*V* measurements and IS in five cells. Figures in the manuscript show illustrative examples of the obtained results and respective simulated data.

[1] I. Podlubny, I. Petrás, T. Skovránek, Fitting of experimental data using Mittag-Leffler function, Proceedings of the 13th International Carpathian Control Conference **2012**, 578.

[2] R. Garrappa, Numerical evaluation of two and three parameter Mittag-Leffler functions, *SIAM J. Numer. Anal.* **2015**, *53*, 1350.